Mon. Not. R. Astron. Soc. **000**, 1–?? (2019) Printed 1 March 2021 (MN LATEX style file v2.2)

Discovery of multiple p-mode pulsation frequencies in the roAp star, HD 86181

Fangfei Shi[1,2], Donald W. Kurtz[3,4], Daniel L. Holdsworth[4], Hideyuki Saio[5], Margarida S. Cunha[6], Huawei Zhang[1,2], Jianning Fu[7], G. Handler[8,9]
[1]*Department of Astronomy, School of Physics, Peking University, Beijing 100871, P. R. China*
[2]*Kavli Institute for Astronomy and Astrophysics, Peking University, Beijing 100871, P. R. China*
[3]*Centre for Space Research, Physics Department, North West University, Mahikeng 2745, South Africa*
[4]*Jeremiah Horrocks Institute, University of Central Lancashire, Preston PR1 2HE, UK*
[5]*Astronomical Institute, Graduate School of Science, Tohoku University, Sendai 980-8578, Japan*
[6]*Instituto de Astrofísica e Ciências do Espaço, Universidade do Porto, CAUP, Rua das Estrelas, PT4150-762 Porto, Portugal*
[7]*Department of Astronomy, Beijing Normal University, Beijing 100875, P. R. China*
[8]*Institut für Astronomie, Universität Wien, Türkenschanzstr$\alpha\beta$e 17, A-1180 Wien, Austria*
[9]*South African Astronomical Observatory, P.O. Box 9, Observatory 7935, South Africa*

Accepted XXX. Received YYY; in original form ZZZ

ABSTRACT
We report the frequency analysis of a known roAp star, HD 86181 (TIC 469246567), with new inferences from TESS data. We derive the rotation frequency to be $\nu_{\rm orb} = 0.48753 \pm 0.00001\,{\rm d}^{-1}$. The pulsation frequency spectrum is rich, consisting of two triplets and one quintuplet, which we interpret to be oblique pulsation multiplets from consecutive, high-overtone dipole, quadrupole and dipole modes. The central frequency of the quintuplet is $232.7701\,{\rm d}^{-1}$. The pulsation amplitude and phase modulation are calculated and fitted with model. The phases of sidelobes, the pulsation phase modulation, and a spherical harmonic decomposition all show this star to be pulsating in a distorted quadrupole mode. Following the oblique pulsator model, we calculate the rotation inclination i and magnetic obliquity β of this star, which provide detailed information about the pulsation geometry. The i and β derived by the best fit of pulsation amplitude and phase modulation through a theoretical model, including the magnetic field effect, slightly differ from those calculated for a pure quadrupole, indicating the contributions from $\ell = 4, 6, 8, ...$ are small. Non-adiabatic models with different envelope convection conditions and physics configurations were considered for this star. Among them, only the model with the minimum radius allowed within the uncertainties can explain the excitation at the observed pulsation frequencies. We also look at other distorted roAp stars and calculate i and β for them. These stars show different behaviours of the coincidence of the pulsation extrema and the light maxima, which is currently not explained.

Key words: stars: oscillations – stars: variables – stars: individual HD 86181 (TIC 469246567; V437 Car)

1 INTRODUCTION

The Ap (chemically peculiar A-type) stars have non-uniform distributions of chemical abundances on their surfaces and strong magnetic fields. These magnetic fields suppress surface convection that then leads to element stratification. For some heavy elements with many absorption features, such as Eu, Sr and Si, the radiation pressure can lift them up to the surface against gravity. These elemental overabundances occur in spots, making Ap stars obliquely rotating variable stars of a class known as α^2 CVn stars (Pyper 1969).

Some cool Ap stars exhibit high-overtone, low-degree pressure pulsation modes with periods between 4.7 and 24 min (frequencies in the range $60 - 300\,{\rm d}^{-1}$; $0.7 - 3.5$ mHz) and photometric amplitudes up to 0.018 mag in Johnson B (Cunha et al. 2019; Kochukhov 2009; Smalley et al. 2015). They are called rapidly oscillating Ap (roAp) stars. These stars show both rotation features with periods of days to decades, and pulsation features.

Stibbs (1950) developed the oblique rotator model of the Ap stars, which accounts well for the form of the rotational magnetic, spectrum, and light variations. Following this model, Kurtz (1982) introduced the oblique pulsator model, which was generalized with the effects of both the magnetic field and rotation taken into account (Kurtz 1982; Dziembowski & Goode 1985; Shibahashi & Takata 1993; Takata & Shibahashi 1994, 1995; Saio & Gautschy 2004; Bigot & Dziembowski 2002; Bigot & Kurtz 2011). According to this model, the pulsation axis is misaligned with the rotation axis,

and generally close to the magnetic axis. When the star rotates, different pulsation aspect is seen along the line of sight, leading to observed amplitude and phase modulation. This modulation can provide information on the geometry of observed pulsations, hence mode identification, which is necessary for asteroseismic inference with forward modelling.

Since the first roAp stars were discovered by Kurtz (1982), 77 rapidly oscillating Ap (roAp) stars have been found (Smalley et al. 2015; Hey et al. 2019; Cunha et al. 2019; Balona, Holdsworth & Cunha 2019). Asteroseismology is a useful method to diagnose stellar structure and interior physics from the evidence of surface pulsations(Cunha, Fernandes & Monteiro 2003). Progress of this research for roAp stars has been hindered by the relatively small number of known stars, and because their rapid pulsation requires dedicated observations at a short enough cadence (Hey et al. 2019; Cunha et al. 2019; Balona, Holdsworth & Cunha 2019).

The space telescopes *Kepler* and TESS provide an opportunity to detect oscillations well below the amplitude threshold of ground-based observations. Both *Kepler* and TESS have short cadence (2-min for TESS and 58.89 s for *Kepler*) observations, but *Kepler* only observed 512 stars in this mode during each observing 'quarter'. However, the standard long cadence sampling frequency of the *Kepler* 30-min observations is generally too low for studying the pulsation of roAp stars.

Murphy, Shibahashi & Kurtz (2013) showed that the Nyquist ambiguity in the LC data can be resolved as a result of the Barycentric corrections applied to *Kepler* time stamps, and Hey et al. (2019) discovered 6 roAp candidates through this method. Compared to the *Kepler* 58.89-s observations, TESS observed many more stars with 2-min observations and long enough observation time. Up to now, 9 new roAp stars have been found from just TESS sectors 1 to 7 (Cunha et al. 2019; Balona, Holdsworth & Cunha 2019).

Before the TESS observations of our target, HD 86181, Kurtz & Martinez (1994) discovered it to be a roAp star from 4.85 hr of ground-based data, which they reported to have a pulsation period of 6.2 min and an amplitude of 0.35 mmag through a Johnson B filter. That period corresponds to a frequency of 2.688 mHz, or $232.26\,\mathrm{d}^{-1}$. We will work in these latter units here for consistency with other TESS roAp star papers. No further studies of the pulsations in HD 86181 have been published.

Parameters for this star are listed in Table 1. The radius was estimated from $L = 4\pi\sigma R^2 T_{\rm eff}^4$, and mass from $M/\mathrm{M}_\odot = (L/\mathrm{L}_\odot)^{1/4}$, with the luminosity and effective temperature given by Anders et al. (2019). The typical $T_{\rm eff}$ uncertainty for a star with Gaia DR2+2MASS+AllWISE data in Anders et al. (2019) catalogue is about 300 K. We have checked that other $T_{\rm eff}$ determinations for HD 86181 publish in the literature agree within 300 K with the value provided by Anders et al. (2019) (Trifonov et al. 2020; Gaia Collaboration et al. 2018; Soubiran et al. 2016). Therefore, we shall adopt an uncertainty of 300 K for the model calculations presented in section 8.

2 TESS OBSERVATIONS

HD 86181 was observed by TESS in sectors 9 and 10 in 2-min cadence. The data have a time span of 51.76 d with a centre point in time of $t_0 = \mathrm{BJD}\ 2458569.80077$, and comprise 33832 data points after some outliers were removed. The standard PDC SAP (pre-search data conditioning simple aperture photometry) fluxes provided by MAST (Mikulski Archive for Space Telescopes) were used and corrected by dividing by the median flux separately for each sector. Relative magnitudes were then calculated from the processed fluxes, giving the light curve shown in the top panel of Fig. 1.

Table 1. Parameters of HD 86181.

Apparent V magnitude	9.39	Schöller et al. (2012)
Spectral type	F0 Sr	Schöller et al. (2012)
Parallax (mas)	4.15 ± 0.013	Gaia Collaboration et al. (2020)
Distance (pc)	240.96 ± 0.75	derived from parallax
Luminosity ($\mathrm{L}_\odot$)	8.69 ± 0.05	derived with extinction A_G from Anders et al. (2019)
$T_{\rm eff}$(K)	7474	Anders et al. (2019)
Radius ($\mathrm{R}_\odot$)	1.76	derived from luminosity and $T_{\rm eff}$
Mass ($\mathrm{M}_\odot$)	1.72	derived from luminosity
log g (cm s^{-2})	4.19	derived from mass and radius
Mean longitudinal magnetic field (G)	536 ± 58	Romanyuk & Kudryavtsev (2008)

There are obvious rotational variations from spots, as is typical of the magnetic Ap stars. Within the oblique rotator model, the double wave nature of the rotational variations suggests two principal spots near the magnetic poles and a rotational inclination i and magnetic obliquity β such that both poles are seen over the rotation cycle. This is common in magnetic Ap stars. The high frequency pulsation cannot be seen in this figure at this resolution and with this signal-to-noise ratio.

3 FREQUENCY ANALYSIS

3.1 Rotation frequency analysis

The central time $t_0 = \mathrm{BJD}\ 2458569.80077$ was used to begin the analysis, but later changed to the time of pulsation maximum to test the oblique pulsator model. For the assessment of phase errors with nonlinear least-squares fitting, it is important that the t_0 chosen is near to the centre of the data set. Since frequency and phase are degenerately coupled in the fitting of sinusoids, when t_0 is not the centre of the data set, small changes in frequency result in very large changes in phase, since phase is referenced from t_0.

Using a Discrete Fourier Transform (Kurtz 1985), we calculated the amplitude spectrum of the data in magnitudes, shown in the top panel of Fig. 2. The low frequencies dominate in the spectrum, so we zoom in to both the low frequency range (second panel) and high frequency range (third panel). From the amplitude spectrum at low frequency, the rotational harmonics are clearly seen. Although the highest peak is at $0.97\,\mathrm{d}^{-1}$, considering the phase plot, we derive the rotation frequency to be around $0.48\,\mathrm{d}^{-1}$. Because the variation is a double wave, the second harmonic has the highest amplitude.

A linear least squares fit was calculated to find the best amplitudes and phases of the rotation frequency and its three harmonics, and then a non-linear least square fit to get optimized results. The rotational frequency is derived to be $\nu_{\rm rot} = 0.48753 \pm 0.00001\,\mathrm{d}^{-1}$ ($P_{\rm rot} = 2.05116 \pm 0.00004\,\mathrm{d}$) by dividing the frequency of the highest amplitude second harmonic by two, which has better signal-to-noise ratio. The errors include the variance from the pulsation and from low frequency artefacts, hence are slightly overestimated. The rotation period is short among the known roAp stars, after HD 43226 (Cunha et al. 2019), HD 216641 (Cunha et al. 2019), and HD 6532 (Kurtz et al. 1996a, Kurtz et al. 1996b), which have similar rotation periods of $P_{\rm rot} = 1.71441\,\mathrm{d}$, $P_{\rm rot} = 1.876660\,\mathrm{d}$, and $P_{\rm rot} = 1.944973\,\mathrm{d}$, respectively.

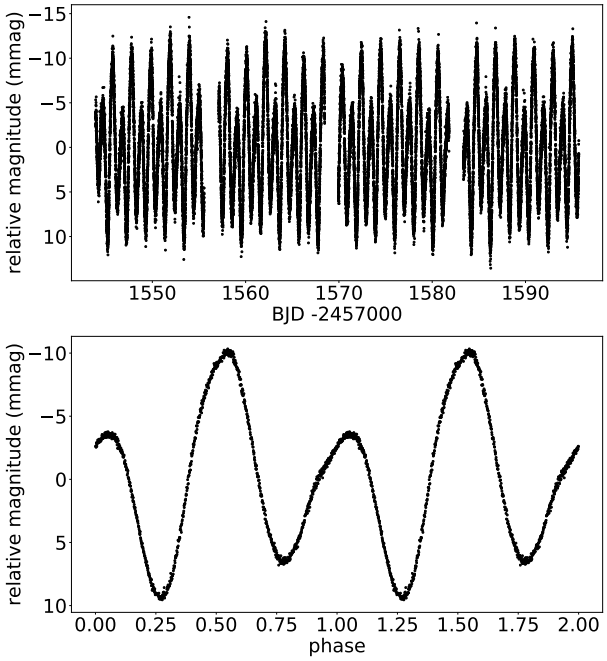

Figure 1. Top: The light curve of HD 86181 showing the rotational variations. Bottom; Phase folded light curve of HD 86181, folded on the rotation period of 2.05116 d; two rotation cycles are shown for clarity. The data are from TESS sectors 9 and 10. The time zero-point, BJD 2458569.26128, is the time of pulsation maximum. The phases are binned every 0.001 phase bin.

3.2 The pulsations

To study the pulsations, a high-pass filter was used to remove the rotational light variations, the drift in the rotation frequency and instrumental artefacts. The high-pass filter was a simple consecutive pre-whitening of low frequency peaks extracted by Fourier analysis until the noise level was reached in the frequency range $0 - 6\,\mathrm{d}^{-1}$. The third panel in Fig. 2 shows the amplitude spectrum for the high-pass filtered data. By inspection it can be seen that there is a central quintuplet and two doublets, one at higher and another at lower frequency than the quintuplet. Besides these three groups, five singlets still remain (see the bottom panel of Fig. 2). However, their frequencies are similar to the quintuplet and two doublets within the uncertainties. These may be caused by amplitude or frequency modulation over the time span of the data set, 51.76 d.

To test this, we removed the doublets and singlets from the light curve and fitted ν_1 to sections of the data that are exactly one rotation cycle long and calculated the amplitude and phase. By doing this, the amplitude and phase variations due to oblique pulsation are averaged out, and only long time scale variations are left. Fig. 3 shows there is amplitude and phase variability with time. Since frequency and phase are degenerate, the phase variability indicates frequency variation with time. We conclude that the central quintuplet and two doublets are pulsation signals.

As in the analysis of rotation frequency, linear and non-linear least squares fits were used to get optimised results, which are shown in Table 2. Those show clearly that the quintuplet frequencies are split by exactly the rotation frequency within the uncertainties. In addition to the quintuplet, there are two doublets which are split by $2\nu_{\mathrm{rot}}$, these are sidelobes of two dipole pulsation frequencies that are labeled as ν_2 and ν_3. Thus, the frequency quintuplet sidelobes were next fixed to be equally spaced by the rotation frequency according to the oblique pulsator model, and the zero-point in time was chosen such that the phases of the first pair of sidelobes are the same, then a linear least squares fit was applied to the data with the results show in Table 3.

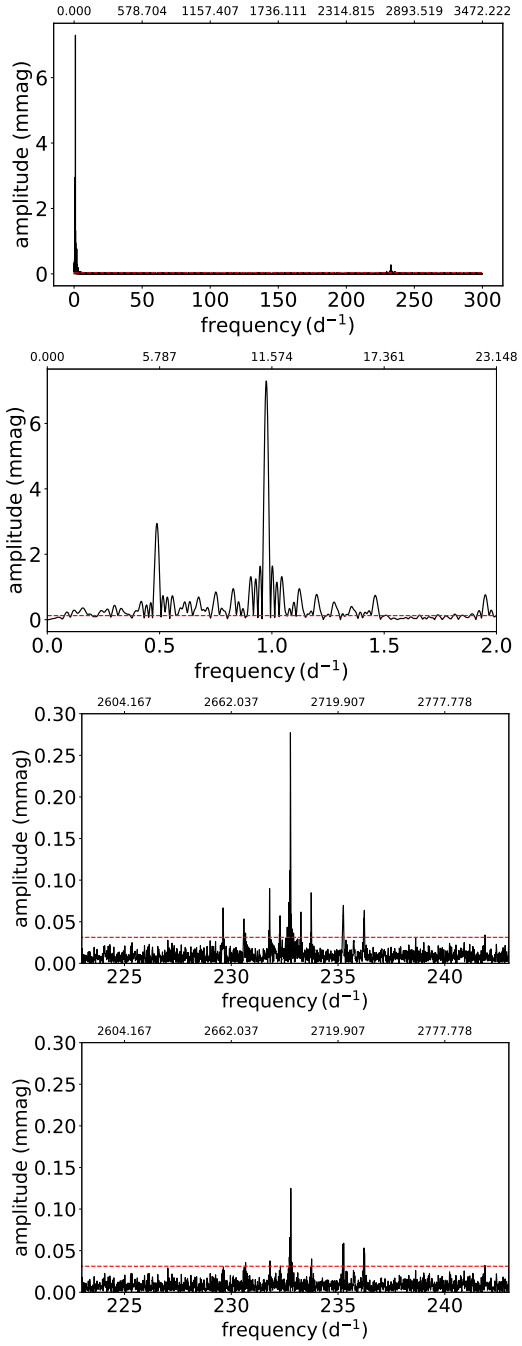

Figure 2. The frequency spectrum of HD 86181. Top: The amplitude spectrum of the S9–10 data out to $300\,\mathrm{d}^{-1}$. The rotational frequencies at low frequency dominate. The pulsation frequencies centred on $232.2\,\mathrm{d}^{-1}$ are difficult to see at this scale. Second: The low frequency rotational harmonics. Third: the pulsation frequencies for the high-pass filtered data. Bottom: The frequency spectrum after the frequencies in Table 2 have been removed. The red horizontal lines are 4 times of noise level. The top x-axis is the corresponding frequency in μHz.

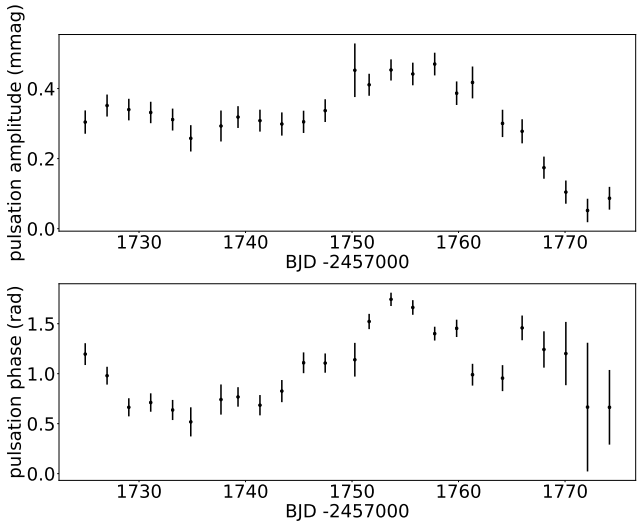

Figure 3. The pulsation amplitude and phase variations of HD 86181 for the dominant quadrupole mode. Top: pulsation amplitude variations as a function of time. Bottom: pulsation phase variations as a function of time.

Table 2. A non-linear least squares fit of the frequency multiplets for HD 86181. The zero point for the phases, t_0 = BJD 2458569.26128, has been chosen to be a time when the first two orbital sidelobes of the quintuplet have equal phase, after the frequency splitting was forced to be equal to exactly the rotation frequency (see Table 3).

	frequency d^{-1}	amplitude mmag ± 0.007	phase radians
ν_{rot}	0.48765 ± 0.00003	2.969	5.829 ± 0.003
$2\nu_{rot}$	0.97506 ± 0.00001	7.296	2.776 ± 0.001
$3\nu_{rot}$	1.46233 ± 0.00013	0.732	0.313 ± 0.013
$4\nu_{rot}$	1.95043 ± 0.00013	0.762	6.178 ± 0.013
$\nu_2 - \nu_{\rm rot}$	229.6162 ± 0.0012	0.059	0.28 ± 0.17
$\nu_2 + \nu_{\rm rot}$	230.5897 ± 0.0014	0.050	0.49 ± 0.20
$\nu_1 - 2\nu_{\rm rot}$	231.7947 ± 0.0008	0.091	6.00 ± 0.11
$\nu_1 - \nu_{\rm rot}$	232.2853 ± 0.0013	0.055	6.27 ± 0.18
ν_1	232.7701 ± 0.0003	0.273	6.24 ± 0.04
$\nu_1 + \nu_{\rm rot}$	233.2587 ± 0.0011	0.062	6.17 ± 0.16
$\nu_1 + 2\nu_{\rm rot}$	233.7438 ± 0.0008	0.080	0.14 ± 0.12
$\nu_3 - \nu_{\rm rot}$	235.2495 ± 0.0010	0.071	6.11 ± 0.14
$\nu_3 + \nu_{\rm rot}$	236.2261 ± 0.0012	0.063	5.94 ± 0.16

3.3 Pulsation amplitude and phase modulation

To study the rotation modulation of the pulsation amplitudes and phases, the light curve was divided into 217 segments each containing 50 pulsation cycles, thus each segment had a time span of 0.21d, or 0.1 of a rotation cycle. Linear least-squares fitting was applied to these segments at fixed frequency, $\nu_1 = 232.7701\,d^{-1}$ to calculate the pulsation amplitude and phase as a function of rotation phase. Fig. 4 shows these modulations along with the rotation light variations for comparison.

The maxima of the pulsation amplitude depend on the aspect of the pulsation axis, while the light extrema depend on the spots. Since both are related to the magnetic field, it is normal that the pulsation maxima occur more or less simultaneously with the light

Table 3. A least squares fit of the frequency multiplets for HD 86181, where the frequency splitting of the rotational sidelobes has been forced to be exactly the rotation frequency. The zero point for the phases, t_0 = BJD 2458569.26128, has been chosen to be a time when the first two orbital sidelobes of the quintuplet have equal phase. It can be seen that all of the phases for the quintuplet are equal within the uncertainties.

	frequency d^{-1}	amplitude mmag ± 0.007	phase radians
$\nu_2 - \nu_{\rm rot}$	229.6162	0.058	0.25 ± 0.11
$\nu_2 + \nu_{\rm rot}$	230.5913	0.049	0.40 ± 0.14
$\nu_1 - 2\nu_{\rm rot}$	231.7950	0.091	-0.26 ± 0.07
$\nu_1 - \nu_{\rm rot}$	232.2826	0.053	-0.13 ± 0.12
ν_1	232.7701	0.273	-0.05 ± 0.02
$\nu_1 + \nu_{\rm rot}$	233.2576	0.061	-0.13 ± 0.11
$\nu_1 + 2\nu_{\rm rot}$	233.7452	0.080	0.14 ± 0.08
$\nu_3 - \nu_{\rm rot}$	235.2494	0.071	-0.13 ± 0.09
$\nu_3 + \nu_{\rm rot}$	236.2245	0.063	-0.11 ± 0.11

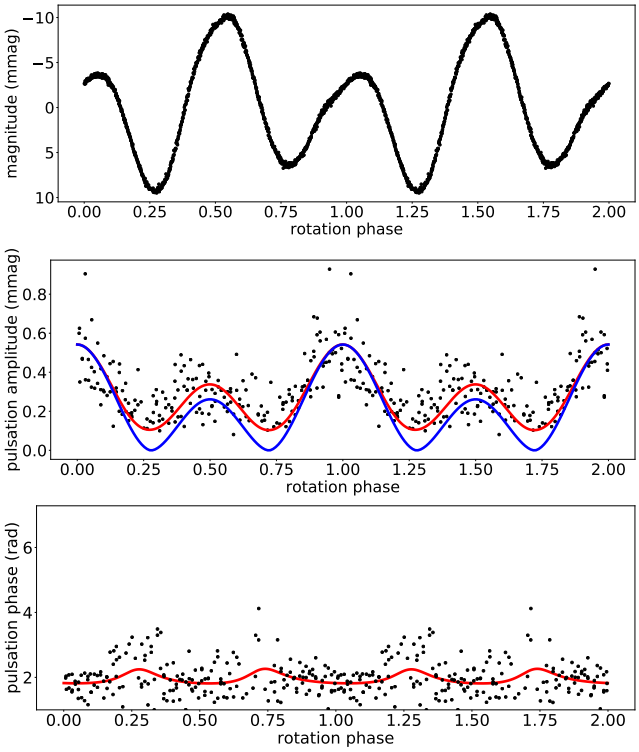

Figure 4. The pulsation modulation of HD 86181. Top: The phase folded rotation light curve. Middle: pulsation amplitude variations as a function of rotation phase. Amplitude points with 1σ errors greater than 0.12 mmag are not plotted here. Bottom: pulsation phase variations as a function of rotation phase. Phase points with 1σ errors greater than 0.8 rad are not plotted here. The red lines are theoretical amplitude modulation modeled following Kurtz (1992) with the components from Table 4. The blue line was calculated based on an oblique pure quadruple mode (see section 4). Two rotation cycles are shown. The time zero-point is t_0 = BJD 2458569.26128.

extrema. Which of the spot extrema coincides with the pulsation maxima depends on the passband of the observations, since the rotational light variations are often in antiphase between blue and red passbands for α^2 CVn stars, as a consequence of the increased temperature gradient in the spots caused by line blocking.

For HD 86181, pulsation amplitude maximum coincides with the secondary maximum of light curve, and after half a cycle, the secondary maximum of pulsation amplitude coincides with the maximum of the light curve. For a pure quadrupole pulsator, the intrinsic pulsation amplitude peaks at both pulsation poles and at the equator. The pulsation maximum at the poles is twice that at the equator, but with inverse phase. We assume the maximum of pulsation amplitude is generated at the pole, while the secondary maximum by equator. This assumption is verified with the the oblique pulsator model below. For Ap stars spots are usually formed close to the poles, so we assume that in the case of HD 86181 here.

At rotation phase 0, which we chose to be the time of pulsation maximum for the quadrupole mode, we see that the spots show the secondary rotational light maximum. In contrast, for another roAp star with a quadrupole mode, KIC 10685175, the maximum of the pulsation amplitude coincides with the minimum of the rotational light (Shi et al. 2020) (Fig. 5). Whether the maximum of pulsation amplitude coincides with the maximum or minimum of the rotational variations is also affected by the positions of the spots, the temperature gradient in the atmosphere, the optical depth of the observations in different passbands and other factors. The difference needs further explanation.

The pulsation phase as a function of rotation does not show a π-rad phase reversal expected at the times of amplitude minima, although the pulsation phase is perturbed at those times. This then argues for a distorted quadrupole mode, and this is similar to what is observed in other the roAp stars with well-studied quadrupole modes (Holdsworth, Saio & Kurtz 2019; Holdsworth et al. 2018b,c,a, 2014; Kurtz et al. 1996b; Holdsworth et al. 2017). The comparison with other distorted pulsators will be discussed at section 9.

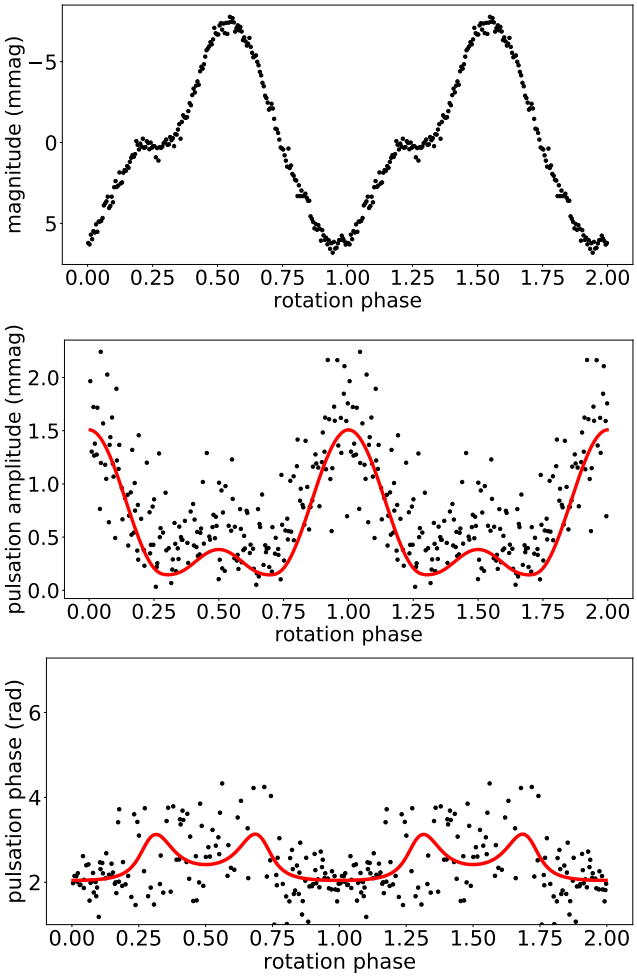

Figure 5. Same as Fig. 4 for KIC 10685175. The time zero-point is t_0 = BJD 2458711.21931.

4 OBLIQUE PULSATOR MODEL

For a normal quadrupole pulsator, with eqns 8 and 10 from Kurtz (1992):

$$\frac{A_{+1}+A_{-1}}{A_0} = \frac{12\sin\beta\cos\beta\sin i\cos i}{(3\cos^2\beta-1)(3\sin^2 i-1))} \quad (1)$$

and

$$\frac{A_{+2}+A_{-2}}{A_0} = \frac{3\sin^2\beta\sin^2 i}{(3\cos^2\beta-1)(3\sin^2 i-1))}. \quad (2)$$

Dividing the two equations leads to a standard constraint for oblique pulsators:

$$\tan i\tan\beta = 4\frac{A_{+2}+A_{-2}}{A_{+1}+A_{-1}}. \quad (3)$$

We can calculate the rotation inclination i and magnetic oblique β of a quadrupole pulsator. Even if this is not the pure case, the results can provide us some information about the geometry of the mode.

The determination of $\tan i\tan\beta$ in a similar manner to eqn 3 for quadrupole modes, is all that can be derived to constrain the geometry of a dipole mode in an oblique pulsator. However, for a normal quadrupole mode, eqns 1 and 2 provide two equations in two unknowns, allowing us nearly uniquely to derive values for i and β. From eqns 1 and 3 we find $i = 84.4°$, $\beta = 30.18°$, or vice versa, for HD 86181.

For an axisymmetric quadrupole mode, the pulsation amplitude at the poles is twice that at the equator and in antiphase. Maximum pulsation amplitude for the angles determined above comes when $i-\beta = 54.22°$. Since the surface nodes for an $\ell = 2, m = 0$ quadrupole lie at co-latitudes $\pm 54.7°$, at the time of pulsation maximum the pole is inclined $i - \beta = 54.22°$ to the line of sight, one surface node is tangent to the lower limb of the star, and the other surface node is over the the top limb. Hence we are seeing only the pulsation polar cap at that time. Half a rotation later, $i + \beta = 114.58°$; i.e., the pole we were seeing is now on the other side of the star. The second pole has come into view, but is at poorer viewing aspect, being inclined $65.42°$ to the line of sight. That then puts one of the surface nodes close to the line of sight, i.e. $65.42 - 54.22 = 11.2°$. Hence much of the visible hemisphere is dominated by the equatorial region.

For the pure oblique quadruple mode, with the angles and the pulsation amplitude distribution on surface: $\frac{1}{2}(3\cos^2\theta - 1)$, where θ is co-latitude, the angle to the poles, we can calculate the integral pulsation amplitude at any time during a rotation cycle. The sphere surface of the star is divided to grids, and at a given time, with the formula, the pulsation amplitude of each place on the grid can be calculated. Then the integrated and projected surface pulsa-

Table 4. Top set: The decomposition result for HD 86181 for rotation phase 0. Components of the spherical harmonic series description of the pulsation for $i = 84.4°$ and $\beta = 30.18°$ for the frequencies amplitudes, and phases from Table 2, with $t_0^{\phi_{rot}=0}$ = BJD 2458569.26128. Bottom set: The decomposition result for HD 86181 for rotation phase 0.5. Components of the spherical harmonic series description of the pulsation for $i = 84.4°$ and $\beta = 30.18°$ for the frequencies, amplitudes and phases from Table 2, with $t_0^{\phi_{rot}=0.5}$ = BJD 2458569.01745.

ℓ	$A_{-2}^{(\ell)}$ (mmag)	$A_{-1}^{(\ell)}$ (mmag)	$A_0^{(\ell)}$ (mmag)	$A_{+1}^{(\ell)}$ (mmag)	$A_{+2}^{(\ell)}$ (mmag)	ϕ (rad)
2	0.093	0.060	−0.278	0.056	0.081	-0.322
1		0.015	0.005	0.014		1.962
0			0.542			-0.204
2	0.093	0.060	−0.278	0.056	0.081	2.703
1		0.031	0.022	0.099		0.597
0			0.442			2.151

tion amplitude can be derived. The limb-darkening model for TESS (Claret 2018) is used here. The results are shown as the blue curves in Fig. 4. The maximum of integral pulsation amplitude is fixed to be the same as the one fitted.

5 SPHERICAL HARMONIC DECOMPOSITION

Using the technique of Kurtz (1992), the quintuplet for HD 86181 can be decomposed into a spherical harmonic series. This was done using the frequencies, amplitudes and phases from Table 3. In order to interpret the two maximum pulsation amplitudes, we calculated the decomposition with the time zero point $t_0^{\phi_{rot}=0}$ = BJD 2458569.26128 (rotation phase 0) and a half of rotation cycle earlier , $t_0^{\phi_{rot}=0.5}$ = BJD 2458569.01745 (rotation phase 0.5), which refer respectively to the time of pulsation amplitude maximum and secondary maximum. The results are shown in Table 4.

In recent works, we correct a small error in the decomposition code. The original code used to calculate the decomposition of HD 6532 (Kurtz et al. 1996b) and several stars mistook equations (8) and (10) in Kurtz (1992). In order to check how much the fit modulation curves will change after the correction, we compare the results before and after the correction. The changes did not bring very large differences to the final fit curves. The comparison of HD 6532 is shown in Fig. 6 as an example.

The decomposition components of HD 86181 show that at phase = 0, there is almost no contribution from the dipole $\ell = 1$ component, and the sum of quadrupole contribution at that phase is only 0.034 mmag – almost nothing comparing to strong radial contribution, which means that the polar amplitude is increased and the equatorial amplitude is reduced compared to a pure quadrupole mode. While at phase 0.5, the dipole $\ell = 1$ component contributes significantly to the quadrupole component. These results verify the assumption that the pulsation amplitude maximum comes from poles, while the secondary maximum from equator.

As an example, we estimate the maximum at phase 0. The quadrupole and radial components then have similar phases, so they add at the time of amplitude maximum. The dipole mode ($\ell = 1$) is negligible, so the pulsation amplitude is $A = 0.542 + 0.093 + 0.060 - 0.278 + 0.056 + 0.081 = 0.559$ mmag, which fits the pulsation phase plot well. Of course, the decomposition technique

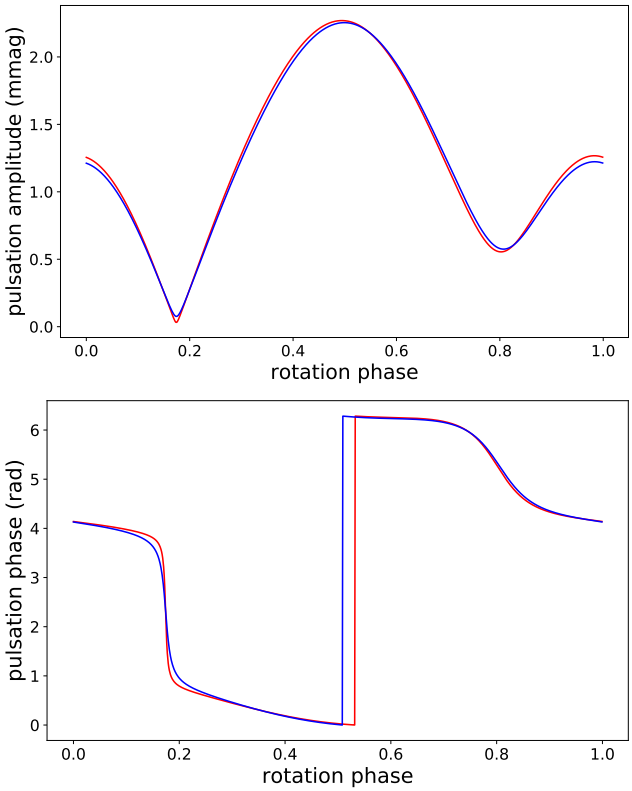

Figure 6. The comparison of the fitted modulation curves of HD 6532 after correction of the code. The red curves are after correction, and the blue curves are original. Top: The pulsation amplitude modulation. Bottom: The pulsation phase modulation.

was designed to fit the data, so it is not a surprise that it does. This discussion is to give a mental picture of why this is so. More precisely, a fit of all three spherical harmonic components taking into account that the exact phases seen in Table 4 gives the fit shown in Fig. 4 as the red curves.

In addition to the quintuplet for HD 86181, there are two doublets. With the i and β derived, we derive $\tan i \tan \beta = 6.05$. For dipoles that gives

$$\frac{A_{+1} + A_{-1}}{A_0} = 6.05. \quad (4)$$

We therefore expect to see triplets with very small central components at ν_2 and ν_3, with amplitudes only about 0.02 mmag, which is at the detection limit for these data. This supports the identification of ν_2 and ν_3 as dipole modes, and it is therefore no surprise that we see doublets separated by twice the rotation frequency.

6 THE LARGE SEPARATION AND ACOUSTIC CUT-OFF FREQUENCY

From the result above we can then calculate that $\nu_2 = 230.103\,\mathrm{d}^{-1}$ and $\nu_3 = 235.737\,\mathrm{d}^{-1}$. That then gives the mode frequency separations to be $\nu_1 - \nu_2 = 2.668\,\mathrm{d}^{-1}$ = 30.87 μHz, and $\nu_3 - \nu_1 = 2.967\,\mathrm{d}^{-1}$ = 34.32 μHz. Using the radius and mass from Table 1, determined using the luminosity and effective temperature from Anders et al. (2019), and the value of the solar large frequency separation $\Delta\nu_\odot = 134.88$ μHz (Huber et al. 2011), through $\Delta\nu \propto$

$\sqrt{\frac{g}{R}}$, we estimate $\Delta\nu/2 = 36.4\,\mu$Hz, which is consistent with the observations.

In roAp stars part of the pulsation mode energy can be refracted back into the star by the influence of the magnetic field, even when the frequency of the mode is above the acoustic cut-off frequency, ν_{ac} (Sousa & Cunha 2008; Quitral-Manosalva, Cunha & Kochukhov 2018). Therefore, there is no reason to assume that very high frequency modes will not be observed in these pulsators. Nevertheless, theory predicts that the excitation by the opacity mechanism takes place in a frequency range that is close to, but does not exceed the cut-off frequency and, thus, that an alternative excitation mechanism would be required to excite modes of yet higher frequencies (Cunha et al. 2013). It is therefore of interest to estimate the cut-off frequency in HD 86181 based on the star's global properties. Using the mass, radius and the effective temperature in solar values in Table 1, and the scaling relation $\nu_{ac} \propto g/\sqrt{T_{\rm eff}}$, we find that in HD 86181 $\nu_{ac} \approx 2.58$ mHz, which is lower than the observed mode frequencies, around 2.73 mHz.

7 MODELLING OBLIQUE QUADRUPOLE PULSATIONS DISTORTED BY DIPOLE MAGNETIC FIELDS

In this section, we present comparisons of the observed amplitude and phase modulations of HD 86181 with a quadrupole pulsation calculated by the method of Saio (2005) including the effect of a dipole magnetic field. We assume that the pulsations in roAp stars are axisymmetric with the pulsation axis aligned with the axis of the dipole magnetic field. The strength of the field is denoted by $B_{\rm p}$, the magnetic field strength at the poles.

In the presence of a magnetic field, the pulsation frequency is modified only slightly (see Fig. 7), while the eigenfunction is distorted considerably because the magnetic effect generates $\ell = 0, 4, 6, \ldots$ components of spherical harmonics in addition to the main $\ell = 2$ component. (We have included twelve components; i.e, up to $\ell = 22$.) The eigenfunction gives pulsation amplitude and phase on each point on the surface as a function of the angle from the magnetic (or pulsation) axis. The amplitude/phase distribution can be converted to observational amplitude/phase modulation as a function of rotation phase (see Saio & Gautschy 2004 for details) for a set of (β, i). The method of comparison is also discussed in Shi et al. (2020).

According to the estimated luminosity and $T_{\rm eff}$ listed in Table 1, we select some stellar structure models of 1.65, 1.68 and 1.70 $M_\odot$ as indicated by triangles in the HR diagram of Fig. 8, in which the initial composition $(X, Z) = (0.70, 0.02)$ is adopted, while the helium abundance is assumed to be depleted to 0.01 (mass fraction) in the layers above the second helium ionisation zone (polar model in Balmforth et al. 2001). For a stellar model, we find, firstly without including a magnetic field, a quadrupole mode having a pulsation frequency close to $\nu_1 = 232.77\,{\rm d}^{-1}$. Then, we re-calculate the quadrupole mode by taking into account the effect of an assumed dipole magnetic field of $B_{\rm p}$.

For each case, an appropriate set of (β, i) is determined by fitting the amplitude modulation of HD 86181. Then, the phase modulation is compared with the observations. Generally, for most assumed values of $B_{\rm p}$, the obliquity and inclination angles (β, i) can be determined easily by fitting the predicted amplitude modulation with the observations, while the theoretical phase modulation tends to be very small except for a certain range of $B_{\rm p}$. Fig. 7 shows how theoretical phase modulations change with changing $B_{\rm p}$ for a 1.65 $M_\odot$ model. In this mode, $8 \lesssim B_{\rm p}$/kG $\lesssim 9.5$ gives phase modulations that are consistent with the observed ones. The range of B_p which gives phase modulations consistent with the observed one depends on the assumed mass: e.g., it is $6.5 \lesssim B_{\rm p}$/kG $\lesssim 7.5$ for 1.70 $M_\odot$. The required B_p tends to be smaller in more massive models because the mean density of the envelope is smaller in more massive stars.

Filled triangles in Fig. 8 indicate the loci of models whose amplitude and phase modulations agree with the observed ones of HD 86181; agreements occur if $B_{\rm p} \sim 7-9$ kG is assumed depending on the assumed stellar mass. Among them, the three red triangles denote the models whose large frequency separations agree with that of HD 86181. We have chosen the 1.65-$M_\odot$ model as the best model because the luminosity agrees better than the 1.70-$M_\odot$ model. However, $\log T_{\rm eff} = 3.8527$ ($T_{\rm eff} = 7124$ K) of the best fit model, is somewhat lower than 7474 K listed in Table 1. This $T_{\rm eff}$ value is closer to Smalley et al. (2015)'s $\log T_{\rm eff} = 3.865$, and to $T_{\rm eff} = 7205$ K obtained by Masana, Jordi & Ribas (2006) from 2MASS photometry.

Fig. 10 compares amplitudes of the rotational sidelobes (top), amplitude (middle) and phase (bottom) modulations between the best model with $B_{\rm p} = 9$ kG and HD 86181. As mentioned above $(\beta, i) = (40^\circ, 80^\circ)$ is determined by fitting the amplitude modulation. The (β, i) given by magnetic distortion model are only slightly different from the pure quadrupole pulsator model; also difference from the phase modulation of the quadrupole model is small, which can be attributed to ℓ =4, 6, 8, ...

Frequencies of dipole modes just above and below the quadrupole mode of the best model are 232.31 and 226.68 ${\rm d}^{-1}$, respectively, at $B_{\rm p} = 9.0$ kG, which yield a large frequency spacing of 5.63 ${\rm d}^{-1}$ (or 65.2 μHz), which agrees with the observed large frequency spacing, $\nu_3 - \nu_2 = 5.63$ ${\rm d}^{-1}$ (or 65.2 μHz).[1] We note that models which reasonably reproduce the phase/amplitude modulation and the large frequency spacing of HD86181 at Bp∼9 kG have $\nu_{ac} = 2.0$ mHz (173 ${\rm d}^{-1}$) considerably lower than the observed frequencies, which is consistent with the result in section 6.

8 DRIVING OF PULSATIONS

The driving of pulsations in roAp stars is still a matter of debate. Non-adiabatic pulsation calculations assuming that envelope convection is suppressed by the magnetic field at least in some angular region around the magnetic pole have been reasonably successful in explaining the driving of most oscillations observed in roAp stars through the opacity mechanism acting on the hydrogen ionization region (Balmforth et al. 2001; Cunha 2002). The same model also predicts that very high frequencies may be excited by the turbulent pressure mechanism, a fact that has been suggested to explain the pulsation frequencies observed in the roAp star α Cir (Cunha et al. 2013). In this section we adopt the models discussed in these earlier works to perform theoretical non-adiabatic pulsation calculations for HD 86181.

The analysis follows closely that presented by Cunha et al. (2013). In short, the equilibrium model is derived from the matching of two spherically symmetric models, one with envelope convection suppressed (the polar model) and the other with convection treated according to a non-local mixing length prescription (Spiegel 1963; Gough 1977a) (the equatorial model). It takes as input the

[1] The frequency spacing of this model at $B_{\rm p} = 0$ is 5.55 ${\rm d}^{-1}$ (or 64.2 μHz).

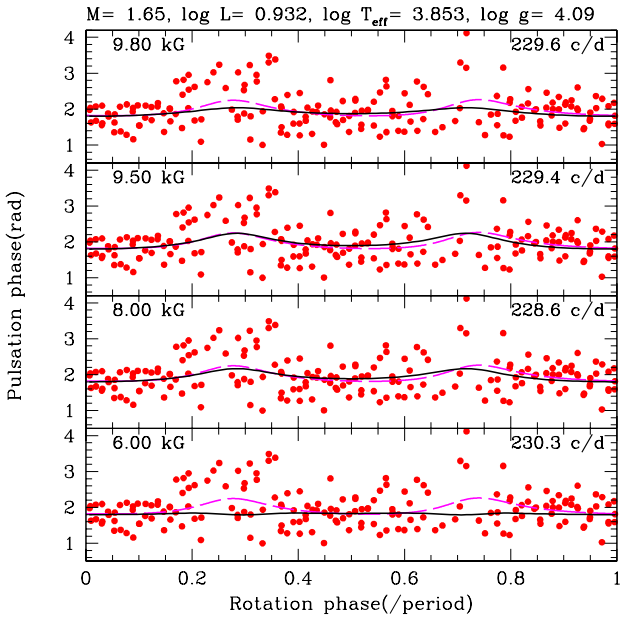

Figure 7. Phase modulations (solid black lines) obtained by assuming various strengths of magnetic fields for the quadrupole mode in the same model shown in Fig. 9. Red dots are observed phase modulations of HD 86181, while dashed magenta lines are the same as the one in the bottom panel of Fig. 9. For all cases, $(\beta, i) = (40°, 80°)$ are adopted, for which the theoretical amplitude modulations are consistent with that of HD 86181, while only $8 \lesssim B_p/kG \lesssim 9.5$ kG give phase modulation comparable with the observed one (see also Fig. 9).

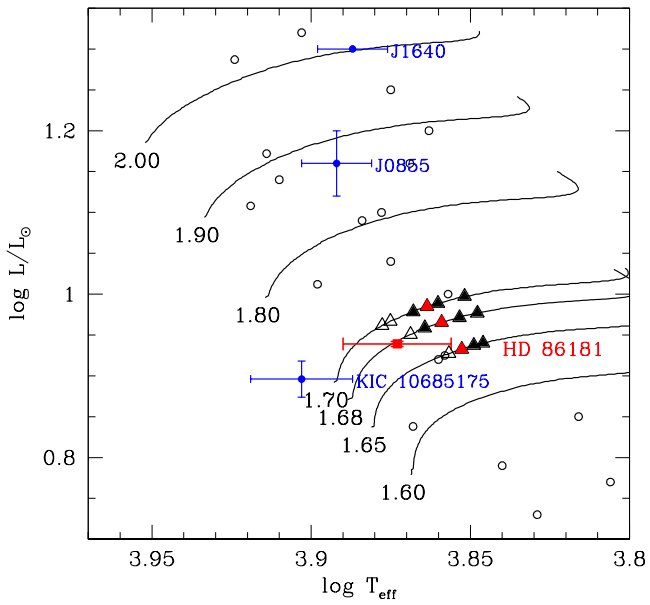

Figure 8. Loci of roAp stars on the HR diagram with some evolutionary tracks with initial composition of $(X, Z) = (0.70, 0.02)$. The number along ZAMS at each track indicates the stellar mass in solar units. HD 86181 and other quadrupole pulsators are shown with error bars. (J1940 is not shown because its location is very close to J1640.) Triangles on 1.70, 1.68 and 1.65 $M_\odot$ tracks indicate the loci of models for which pulsation amplitude phase modulations are calculated; filled (open) triangles indicate models whose phase modulations can (cannot) be fitted with the HD 86181 phase modulation. Red filled triangles indicate models which have large frequency spacings similar to the observed one. Parameters of roAp stars other than HD 86181 are adopted from Holdsworth et al. (2018b).

stellar mass, luminosity, effective temperature, chemical composition (hydrogen, X, and helium, Y, mass fractions) and the parameters associated with convection. The atmosphere is described by a $T - \tau$ relation, which can be chosen amongst different options, with the minimum optical depth, $\tau_{\rm min}$, being an additional input parameter. Finally, helium settling can also be considered both in the polar and in the equatorial regions, following a parametrized description with the surface helium abundance in each region being additional input parameters.

The stability analysis is performed in each region separately and can consider two different options for the surface boundary condition applied at the minimum optical depth, namely, one that guarantees a full reflection of the mode and one that allows waves with frequencies above the acoustic cut-off frequency to propagate. In the equatorial model, the final non-adiabatic solutions are computed using a non-local, time-dependent mixing-length treatment of convection (Gough 1977b; Balmforth 1992). The results from the non-adiabatic analysis in each region can then be combined to derived the growth rates of modes in the model where convection is assumed to be suppressed only in some angular region around the magnetic pole (the composite model). Further details on the models can be found in Balmforth et al. (2001) and references therein.

For each set of (M,L,$T_{\rm eff}$), four different physics configurations were considered by varying different input parameters identified in previous works as having significant impact on the stability results, namely: the minimum optical depth, the outer boundary condition, and the amount of surface helium. Table 5 summarizes the options in each case. Other parameters and physics not mentioned here were fixed following the options adopted in Balmforth et al. (2001).

Fig. 10 shows an example of the results from the stability analysis in blue and red, for polar and equatorial models, respectively, adopting the effective temperature and luminosity in Table 1. Here we plot the relative growth rates η/ω as a function of the cyclic pulsation frequency ν, where η and ω are the imaginary and real parts of the angular eigenfrequency, respectively, and a positive growth rate indicates the mode is intrinsically unstable, thus excited. From the red symbols in the figure we can see that all modes are stable in the equatorial model, independently of the physics configuration adopted. In the polar models (blue symbols), a few modes have positive growth rates at frequencies around 2.2 mHz, for three out of the four cases. Their growth rates are one order of magnitude smaller than the growth rates of the corresponding modes in the equatorial model (in absolute value). This means that envelope convection would need to be almost fully suppressed in order for these modes to be unstable in the composite model (cf. figure 4 of Balmforth et al. 2001). Moreover, these modes have frequencies substantially smaller than those observed in HD 86181, thus, their excitation would not help explain the observed oscillations. In order to explore the impact of the uncertainties in effective temperature and luminosity on the stability analysis, we have considered four additional cases corresponding to the extremes of an uncertainty box defined by $T_{\rm eff} = 7474 \pm 300$ K and $L = 8.69 \pm 0.05\,L_\odot$.

For the model with the smallest radius allowed by these un-

Table 5. Modelling parameters for the cases illustrated in Fig. 10, all computed with $M = 1.72\,\mathrm{M}_\odot$, $T_{\rm eff} = 7474\,\mathrm{K}$, $L = 8.69\,\mathrm{L}_\odot$, $Y = 0.278$, $X = 0.705$.

Model	Polar $Y_{\rm surf}$	Equatorial $Y_{\rm surf}$	$\tau_{\rm min}$	Boundary condition	symbols in Fig. 10
A	0.01	0.278	3.5×10^{-5}	Reflective	circles
B	0.01	0.278	3.5×10^{-4}	Reflective	squares
C	0.01	0.278	3.5×10^{-5}	Transmissive	upward triangles
D	0.1	0.1	3.5×10^{-5}	Reflective	rightward triangles

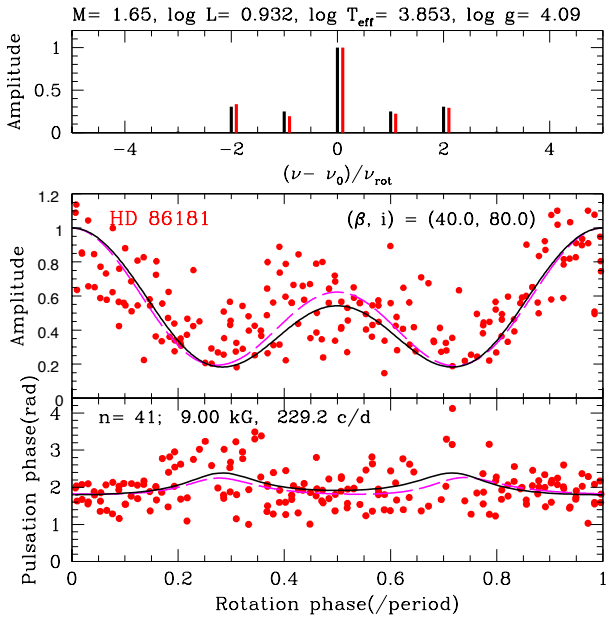

Figure 9. The amplitude spectrum of rotational sidelobes (top panel) and amplitude (middle panel)/phase (bottom panel) modulations of the quadrupole pulsation mode of HD 86181 are shown by red lines or dots. Dashed magenta lines (middle and bottom panels) are obtained from the oblique pulsator model of Kurtz (1992) (red line in Fig. 4). Black lines show the results of a best model of $1.65\,\mathrm{M}_\odot$ with $B_{\rm p} = 9$ kG, for which parameters are shown on the top of the diagram.

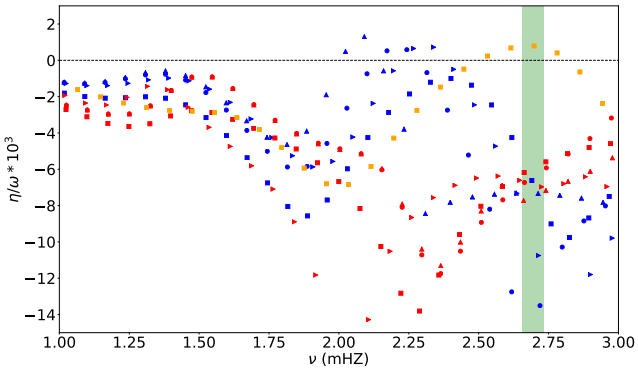

Figure 10. Normalized growth rates for polar (blue and orange symbols) and equatorial (red symbols) regions as function of the cyclic frequency $\nu = \omega/2\pi$. The blue and red symbols are computed with $M = 1.72\,\mathrm{M}_\odot$, $T_{\rm eff} = 7474\,\mathrm{K}$, $L = 8.69\,\mathrm{L}_\odot$, and the orange symbols are computed with $M = 1.72\,\mathrm{M}_\odot$, $T_{\rm eff} = 7774\,\mathrm{K}$, $L = 8.64\,\mathrm{L}_\odot$. Different shape symbols represent different modelling parameters we have used; circles are for model A in Table 5, while squares, upward triangles and rightward triangles for model B, C and D, respectively. Zero growth rate is indicated by the horizontal dashed line and the green shadowed region marks the range of observed frequencies.

certainties, we find that the unstable modes in the polar model shift to the observed frequency range (orange symbols in Fig. 10), while the growth rates of corresponding modes in the equatorial model are still negative and about one order of magnitude larger in absolute value than those of the polar models. So, if envelope convection is suppressed by the magnetic field, the stability results may explain the observed pulsations, but only if the radius of the star is closer to the minimum allowed by the uncertainties in $T_{\rm eff}$ and L.

9 COMPARISON WITH OTHER ROAP STARS WITH DISTORTED MODES

There are 9 roAp stars that are known to pulsate in distorted modes found in the literature and listed in Table 6 with references. Nearly all the quadrupole pulsators are distorted. We calculated values of i and β for pure quadrupole pulsators, and compared them with those derived from models. The differences between our calculations and the models show the degree of distortion. These 9 stars with their pulsation frequency spectra, and the values of i and β, are given in Table 6. The values of i and β can not be calculated without the amplitudes of the second sidelobes, or for dipole modes.

Although some stars have quintuplet sidelobes, they were identified as distorted dipole modes. For these stars, such as HR 3831, HD 99563 and HD 6532, there is clear phase reversal of π radians at the time of pulsation amplitude minimum. Dipole modes can explain these simply. In the case here of HD 86181 we have good mode identification from the triplet-quintuplet-triplet pattern, so we can be more confident of the identifications.

Except for J1640, other stars in Table 6 were all observed by TESS or the K2 mission. In order to compare the modulation behaviour, we also analyse the pulsation amplitude and phase modulations of these stars with the space telescope data (in Appendix A). The pulsation phases of HD 42659, HD 6532 and HD 99563 all show π-rad reversals, which is common for dipole pulsators. J0855 and J1940 show long time scale phase variations which are not found through the ground-based observation. The maximum of the pulsation amplitude can coincide with the maximum (HD 6532, HD 42659, HD 99563, J0855, HD 24355) or the minimum (HD 80316, J1940) of the rotational light variations. Also, the secondary maximum of the pulsation amplitude can also coincide with the maximum (HD 99563, HD 24355) or the minimum (HD 42659, J1940) of the rotational light variations. Since the ground-based observations for roAp stars are mostly carried in the B band where these stars have the maximum pulsation amplitude, the pulsation amplitudes are clearly larger than the space observations which were observed in red-like filters.

Table 6. Basic information for 9 roAp stars pulsating in distorted modes.

ID	pulsation frequency	distorted mode	i, β (degrees) model	i, β (degrees) pure quadrupole	reference
J1640 (2MASS 16400299–0737293)	quintuplet	quadrupole	$(70, 13)$	$(76.69, 12.96)$	Holdsworth et al. (2018b)
J1940 (2MASS J19400781–4420093)	quintuplet	quadrupole	$(84, 30)$	$(83.65, 28.5)$	Holdsworth et al. (2018a)
HD 24355	13 sidelobes	quadrupole	$(45, 77)$	$(26.24, 82.86)$	Holdsworth et al. (2017)
J0855 (TYC 2488-1241-1)	triplet	quadrupole	$(24, 30)$	—	Holdsworth et al. (2018c)
HD 42659	triplet	dipole & quadrupole	$(78, 20)$	—	Holdsworth, Saio & Kurtz (2019)
HD 99563	quintuplet	dipole	—	—	Handler et al. (2006)
HD 6532	quintuplet	dipole	—	—	Kurtz et al. (1996b)
HD 3831	septuplet	dipole	—	—	Kurtz et al. (1997b)
HD 80316	triplet	dipole	—	—	Kurtz et al. (1997a)

Among these stars, HD 99563, J0855, J1940 and HD 24355 have ground-based rotation light curves. HD 99563 was observed in U, B, V, R, I filters, J0855 in B, and J1940 and HD 24355 in the 'WASP-V' filter. For HD 99563, the mean light maxima in the U and B filters occurs at the same time as pulsation amplitude maximum, while in the V, R and I filters, mean light minimum coincides with pulsation amplitude maximum. For J0855, the maximum of pulsation amplitude coincides with mean light minimum. For J1940, the phase difference between the pulsation amplitude maximum and light maximum is about 0.138 rotation periods. Also, for HD 24355, the pulsation amplitude maximum coincides with light maximum (in Appendix B). All of these correlations show that the pulsation axes of these stars must be close to alignment with the abundance spots, which are presumed to be close to the magnetic poles. Whether the pulsation maximum coincides with rotational light maximum or minimum is a function of the depth into the atmosphere that the observations probe – hence the passband of the observations – and the temperature gradient, which itself is a function of the line blocking, hence abundance anomalies.

TIC 350146296 is a new roAp star found in TESS Sectors 1 and 2 data by Cunha et al. (2019). This star shares some similar features to HD 86181. The pulsation spectrum is also rich with a singlet, a triplet, a quintuplet, and another triplet, all split by the rotation frequency. With the rich pulsation spectrum, Cunha et al. also studied the large frequency separation. With the amplitude ratios, the values of $\tan i \tan \beta$ of two triplets and one quintuplet were calculated, but the values of i and β were not specifically calculated from the quadrupole mode. Also, the distortion was not discussed in their work, but the phases of the sidelobes show that there is a little distortion. Following the method in this paper, we derived that $i = 80.86^\circ$ and $\beta = 30.45^\circ$, or vice versa, for this star.

The frequencies of the pulsations observed in TIC 350146296 may be above the star's acoustic cut-off frequency, ν_{ac}. In addition to TIC 350146296 and HD 86181, there are more than a dozen other roAp stars showing pulsation frequencies above the acoustic cut-off frequency, some significantly above ν_{ac}; see, e.g., figure 6 of Holdsworth et al. (2018c).

Since TIC 350146296 was observed by TESS from Sector 1 to 13, and the modulation was not discussed by the previous work, we analyse this star in the same way as above. In order to avoid the ragged peaks in the amplitude spectrum caused by strong modulation, a continuous data set of sufficient length from BJD 2458425 to BJD 2458529 was selected rather than all of the data. More frequencies are found compared to the previous work.

The least squares fit of the frequency multiplets and the modulation of ν_4 are shown in Table 7 and Fig. 11. The pulsation amplitude maximum and secondary maximum coincide with the minimum and secondary maximum of light, which is consistent with KIC 10685175 (Fig. 5) seems to be common for roAp stars observed by TESS.

Table 7. A least squares fit of the frequency multiplets for TIC 350146296. The zero point for the phases, $t_0 = \mathrm{BJD}\ 2458473.52490$, has been chosen to be a time when the first two orbital sidelobes of ν_4 have equal phase.

	frequency d^{-1}	amplitude mmag ± 0.006	phase radians
$\nu_1 - \nu_{\rm rot}$	293.6617	0.033	1.74 ± 0.18
$\nu_1 + \nu_{\rm rot}$	294.4125	0.041	2.04 ± 0.14
$\nu_2 - 2\nu_{\rm rot}$	296.6815	0.031	0.38 ± 0.19
ν_2	297.4323	0.045	0.95 ± 0.13
$\nu_2 + \nu_{\rm rot}$	297.8078	0.013	0.95 ± 0.44
$\nu_3 - \nu_{\rm rot}$	300.6380	0.084	1.44 ± 0.07
ν_3	301.0134	0.034	2.17 ± 0.17
$\nu_3 + \nu_{\rm rot}$	301.3889	0.070	2.06 ± 0.08
$\nu_4 - 2\nu_{\rm rot}$	303.6572	0.068	3.30 ± 0.09
$\nu_4 - \nu_{\rm rot}$	304.0326	0.057	3.81 ± 0.10
ν_4	304.4080	0.170	3.63 ± 0.03
$\nu_4 + \nu_{\rm rot}$	304.7834	0.060	3.81 ± 0.10
$\nu_4 + 2\nu_{\rm rot}$	305.1588	0.049	4.20 ± 0.12
$\nu_5 - \nu_{\rm rot}$	307.4277	0.031	1.38 ± 0.19
ν_5	307.8031	0.019	1.73 ± 0.31
$\nu_5 + \nu_{\rm rot}$	308.1785	0.026	1.93 ± 0.23

The light curve of TIC 350146296 shows a triple bump which is rotational modulation due to multiple spots. The pulsation maxima coincide with the light minimum and the second maximum. The spots are not necessarily situated closed to the pulsation pole. The places, sizes of the spots, and how the spots redistribute the flux all affect the light curves. We need to be careful in interpreting the spot-pulsation maximum coincidences.

10 DISCUSSION AND CONCLUSIONS

We analysed HD 86181 with TESS data, and confirm it as a roAp star. The rotation frequency is derived to be $\nu_{\rm rot} = 0.48765 \pm 0.00003\,\mathrm{d}^{-1}$ ($P_{\rm rot} = 2.0507 \pm 0.0001$ d). The pulsation frequency spectrum is rich, consisting of one triplet, one quintuplet and another triplet. The central frequency of the quintuplet is

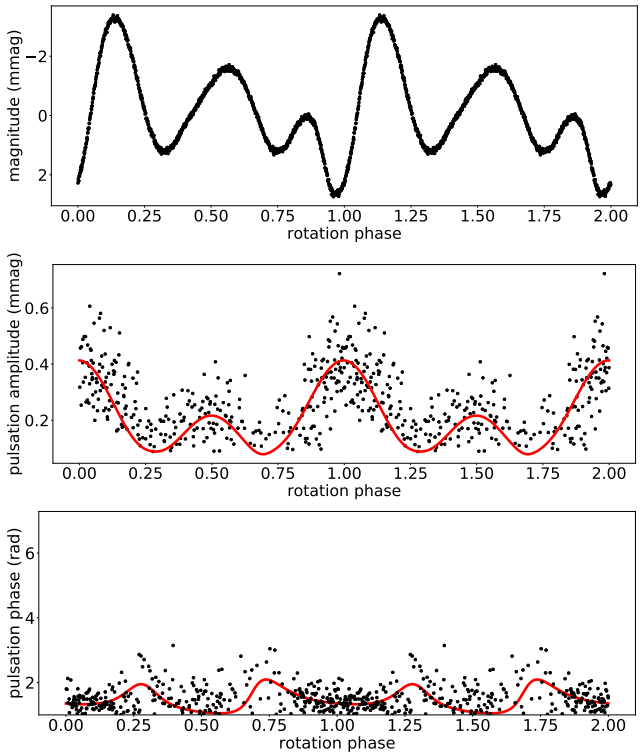

Figure 11. The pulsation modulation of ν_4 of TIC 350146296. To reduce the errors, the other pulsation modes and long time trend have been removed. Top: The phase folded rotation light curve. Middle: pulsation amplitude variations as a function of rotation phase. Amplitude points with 1σ errors greater than 0.12 mmag are not plotted here. Bottom: pulsation phase variations as a function of rotation phase. Phase points with 1σ errors greater than 0.8 rad are not plotted here. The red lines are theoretical amplitude and phase modulation modelled following Kurtz (1992) with the components of quintuplets of ν_4 from Table 3. Two rotation cycles are shown. The time zero-point is $t_0 = \mathrm{BJD}\ 2458473.52490$.

232.7701 d^{-1} (2.694 mHz). The amplitudes of the two triplet central frequencies are too small to be observed, but we calculate them to be 230.1028 d^{-1} (2.663 mHz) and 235.7361 d^{-1} (2.728 mHz).

Pulsation amplitude and phase modulation as a function of rotation phase were calculated. Two maxima of light can be seen which indicates we can see the two poles. The pulsation modulation and pulsation phases of the sidelobes show that KIC 10685175 is a weakly distorted quadrupole pulsator. However, unlike the KIC 10685175, a roAp star observed by TESS, two pulsation amplitude maxima coincide with two maxima of light. Since the two pulsation amplitude maxima correspond to the pole and equator, but spots are assumed to situate only near the pole, we expect two pulsation amplitude maxima coincide with one maximum and one minimum of the light. This unusual behaviour needs more explanation.

We calculated the rotation inclination, i, and magnetic obliquity, β for HD 86181, which provided detailed information of geometry and we used those with a spherical harmonic decomposition to better understand the pulsation geometry and the distortion from a pure quadrupole mode.

Models considering the dipole magnetic field distortion were calculated and compared with the observed observed amplitude and phase modulation. The best fit model gives $B_\mathrm{p} = 9$ kG and $(\beta, i) = (40°, 80°)$. The (β, i) given by magnetic distortion model are only slightly different from the pure quadrupole pulsator model, also the difference from the phase modulation of the quadrupole model is small, which can be attributed to small $\ell = 4, 6, 8, ...$ The pulsation frequency and the large frequency spacing given by this model are comparable with the observation.

To explain the driving mechanism of this star, two non-adiabatic models, one with envelope convection suppressed (the polar model) and another considering convection (the equatorial model) were applied for HD 86181. Changing physical configurations as input, we find for some polar models, a few modes excited. For these excited modes to be within the range of observed frequencies, the radius of the star needs to be close to the lower limit allowed by the uncertainties in effective temperature and luminosity.

The rich pulsation frequency spectrum let us study the large frequency separation, $\Delta\nu$. The $\log g$ derived from $\Delta\nu$ is consistent with the value in the literature. The acoustic cut-off frequency ν_{ac} of this star is lower than the observed mode frequencies, which indicates that the frequencies may be excited by a process different than the opacity mechanism.

We also analysed TIC 350146296, which has rich pulsation frequencies, and all the distorted roAp stars as comparisons, and calculate the values of i and β for some of them. The modulation curves of these stars show different coincidence of the pulsation extrema and the light maximum, which is currently difficult to explain.

REFERENCES

Anders F. et al., 2019, A&A, 628, A94
Balmforth N. J., 1992, MNRAS, 255, 603
Balmforth N. J., Cunha M. S., Dolez N., Gough D. O., Vauclair S., 2001, MNRAS, 323, 362
Balona L. A., Holdsworth D. L., Cunha M. S., 2019, MNRAS, 487, 2117
Bigot L., Dziembowski W. A., 2002, A&A, 391, 235
Bigot L., Kurtz D. W., 2011, A&A, 536, A73
Claret A., 2018, A&A, 618, A20
Cunha M. S., 2002, MNRAS, 333, 47
Cunha M. S., Alentiev D., Brandão I. M., Perraut K., 2013, MNRAS, 436, 1639
Cunha M. S. et al., 2019, MNRAS, 487, 3523
Cunha M. S., Fernandes J. M. M. B., Monteiro M. J. P. F. G., 2003, MNRAS, 343, 831
Dziembowski W., Goode P. R., 1985, ApJ, 296, L27
Gaia Collaboration et al., 2018, A&A, 616, A1
Gaia Collaboration, Brown A. G. A., Vallenari A., Prusti T., de Bruijne J. H. J., Babusiaux C., Biermann M., 2020, arXiv e-prints, arXiv:2012.01533
Gough D., 1977a, The current state of stellar mixing-length theory, Spiegel E. A., Zahn J. P., eds., Vol. 71, pp. 15–56
Gough D. O., 1977b, ApJ, 214, 196
Handler G. et al., 2006, Monthly Notices of the Royal Astronomical Society, 366, 257???266
Hey D. R. et al., 2019, MNRAS, 488, 18
Holdsworth D. L. et al., 2018a, MNRAS, 473, 91
Holdsworth D. L., Kurtz D. W., Smalley B., Saio H., Handler G., Murphy S. J., Lehmann H., 2017, in European Physical Journal Web of Conferences, Vol. 160, European Physical Journal Web of Conferences, p. 03004
Holdsworth D. L., Saio H., Bowman D. M., Kurtz D. W., Sefako

R. R., Joyce M., Lambert T., Smalley B., 2018b, MNRAS, 476, 601
Holdsworth D. L., Saio H., Kurtz D. W., 2019, MNRAS, 489, 4063
Holdsworth D. L., Saio H., Sefako R. R., Bowman D. M., 2018c, MNRAS, 480, 2405
Holdsworth D. L., Smalley B., Kurtz D. W., Southworth J., Cunha M. S., Clubb K. I., 2014, MNRAS, 443, 2049
Huber D. et al., 2011, ApJ, 743, 143
Kochukhov O., 2009, Communications in Asteroseismology, 159, 61
Kurtz D. W., 1982, MNRAS, 200, 807
—, 1985, MNRAS, 213, 773
—, 1992, MNRAS, 259, 701
Kurtz D. W., Marang F., van Wyk F., Roberts G., 1996a, MNRAS, 280, 1
Kurtz D. W., Martinez P., 1994, Information Bulletin on Variable Stars, 4013, 1
Kurtz D. W., Martinez P., Koen C., Sullivan D. J., 1996b, MNRAS, 281, 883
Kurtz D. W., Martinez P., Tripe P., Hanbury A. G., 1997a, MNRAS, 289, 645
Kurtz D. W., van Wyk F., Roberts G., Marang F., Handler G., Medupe R., Kilkenny D., 1997b, MNRAS, 287, 69
Masana E., Jordi C., Ribas I., 2006, A&A, 450, 735
Murphy S. J., Shibahashi H., Kurtz D. W., 2013, MNRAS, 430, 2986
Pyper D. M., 1969, ApJS, 18, 347
Quitral-Manosalva P., Cunha M. S., Kochukhov O., 2018, MNRAS, 480, 1676
Romanyuk I. I., Kudryavtsev D. O., 2008, Astrophysical Bulletin, 63, 139
Saio H., 2005, MNRAS, 360, 1022
Saio H., Gautschy A., 2004, MNRAS, 350, 485
Schöller M., Correia S., Hubrig S., Kurtz D. W., 2012, A&A, 545, A38
Shi F., Kurtz D., Saio H., Fu J., Zhang H., 2020, ApJ, 901, 15
Shibahashi H., Takata M., 1993, PASJ, 45, 617
Smalley B. et al., 2015, MNRAS, 452, 3334
Soubiran C., Le Campion J.-F., Brouillet N., Chemin L., 2016, A&A, 591, A118
Sousa S. G., Cunha M. S., 2008, MNRAS, 386, 531
Spiegel E. A., 1963, ApJ, 138, 216
Stibbs D. W. N., 1950, MNRAS, 110, 395
Takata M., Shibahashi H., 1994, PASJ, 46, 301
—, 1995, PASJ, 47, 219
Trifonov T., Tal-Or L., Zechmeister M., Kaminski A., Zucker S., Mazeh T., 2020, A&A, 636, A74

ACKNOWLEDGEMENTS

This work was funded by the National Key R & D Program of China under grant No.2019YFA0405504 and the National Natural Science Foundation of China (NSFC) under grants No. 11973001, No. 11833002, No. 12090040 and No. 12090042. This work includes data collected by the TESS mission. Funding for the TESS mission is provided by the NASA Explorer Program.

A THE MODULATIONS OF DISTORTED ROAP STARS BASED ON SPACE OBSERVATION.

In the appendix, the rotation light curves, and the pulsation amplitude and phase variations with rotation of the 9 distorted roAp stars mentioned in section 9 are shown.

We collected the space- and ground-based observation data for these distorted roAp stars, and analyzed the pulsation amplitude and phase modulations for them as we have done for HD 86181. Since the ground-based observations were always carried out in the B band, the pulsation amplitudes are larger than for the space observations. This is clearly seen in Figs 12–20. From the comparison, we can see the behaviours of the maxima of rotation light curves and the extrema of the pulsation amplitude modulation curves.

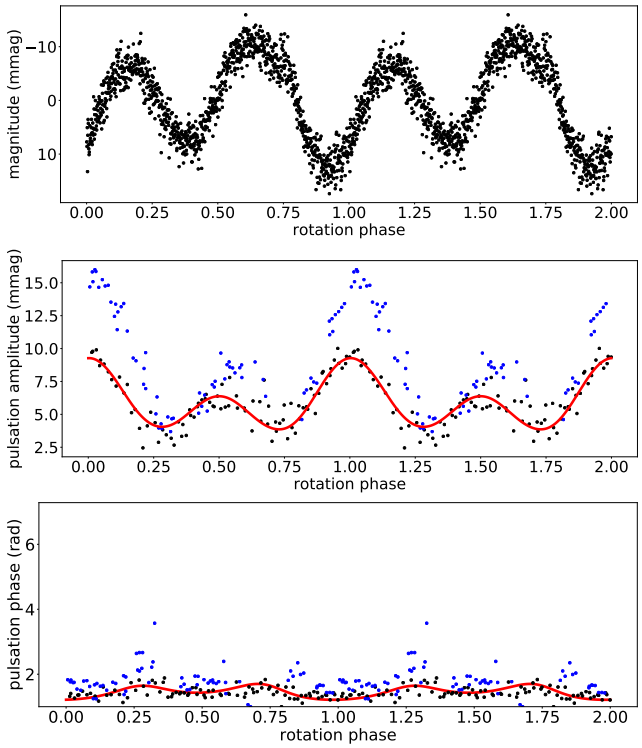

Figure 12. The same as Fig. 4 but for J1940. The black points are the data from TESS sector 13 observation and the blue points are from ground-based observations (Holdsworth et al. 2018a).

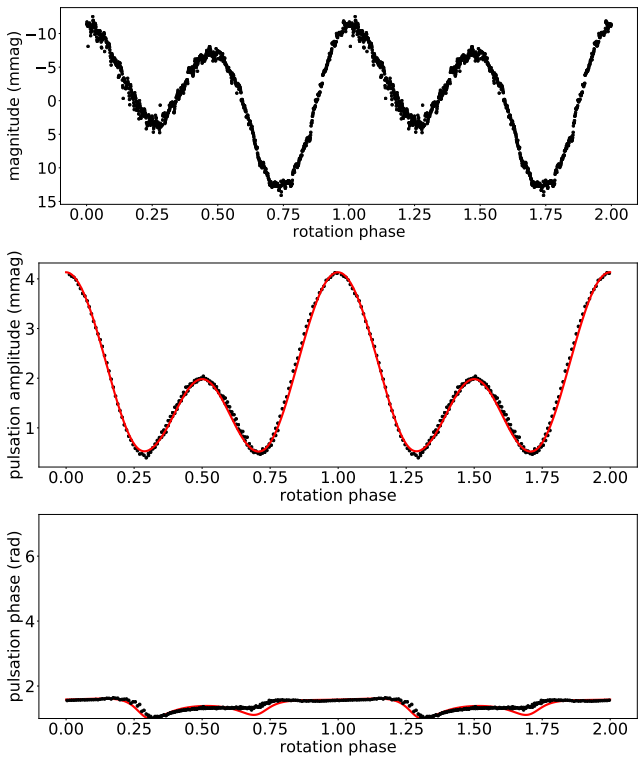

Figure 13. The same as Fig. 4 but for HD 24355. The black points are the data from K2 observations. There are no ground-based observations for this star.

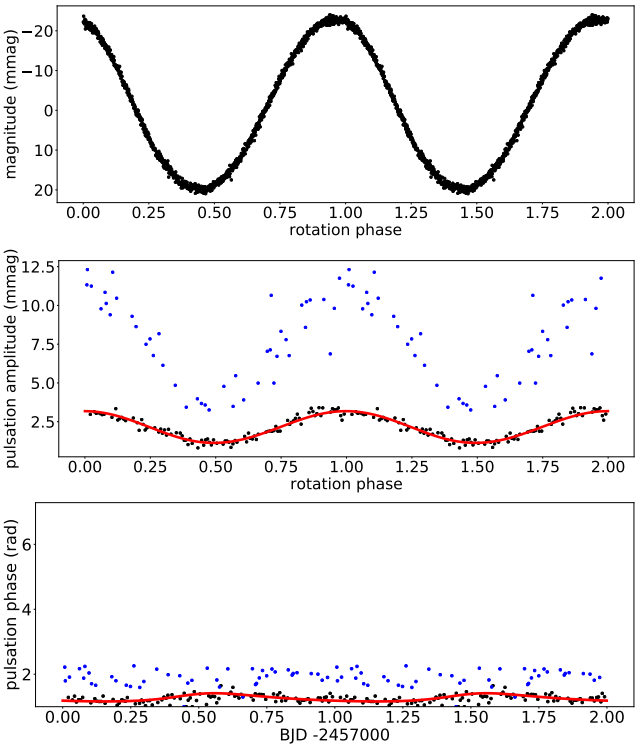

Figure 14. The same as Fig. 4 but for J0855. The bottom panel shows the pulsation phases change with time instead of rotation phase. The black points are the data from TESS sector 21 observation and the blue points are from ground-based observation (Holdsworth et al. 2018c).

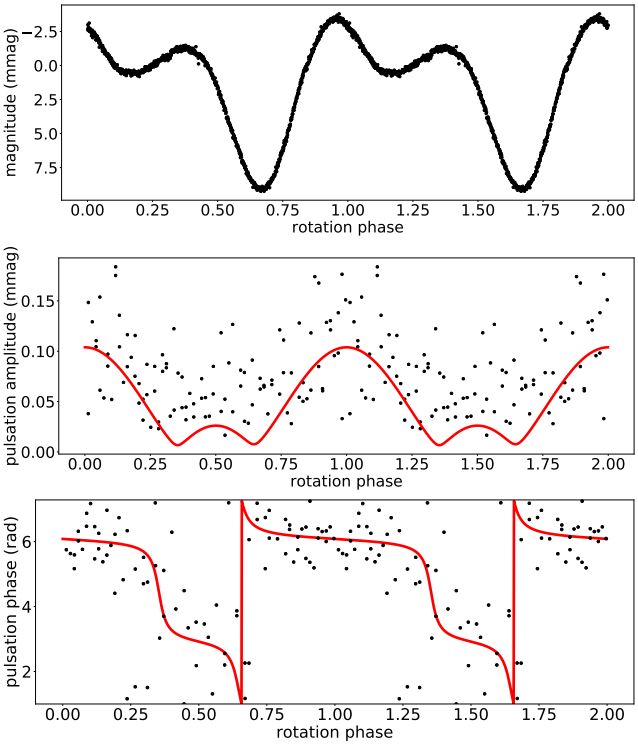

Figure 15. The same as Fig. 4 but for HD 42659. The data are from TESS sector 6 observations. There are no ground-based data for this star.

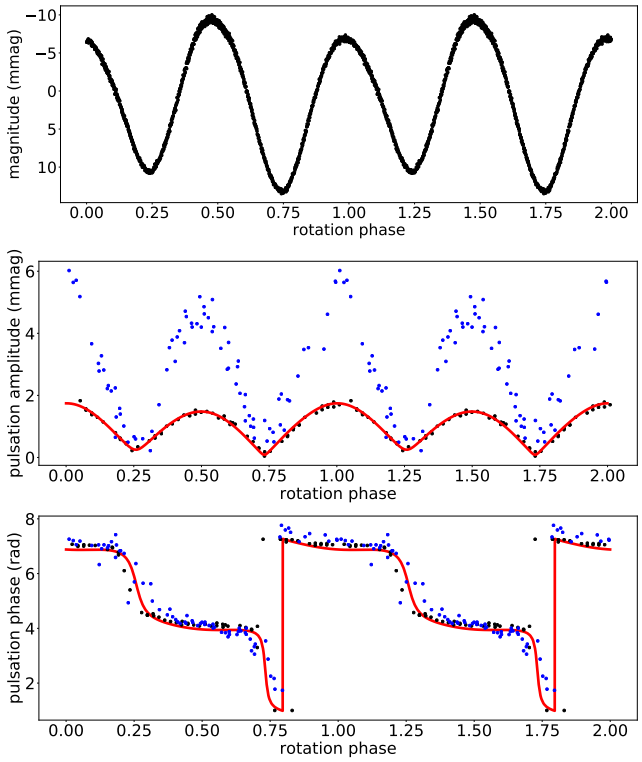

Figure 16. The same as Fig. 4 but for HD 99563. The black points are the data from TESS sector 9 observation and the blue points are from ground-based observation (Handler et al. 2006).

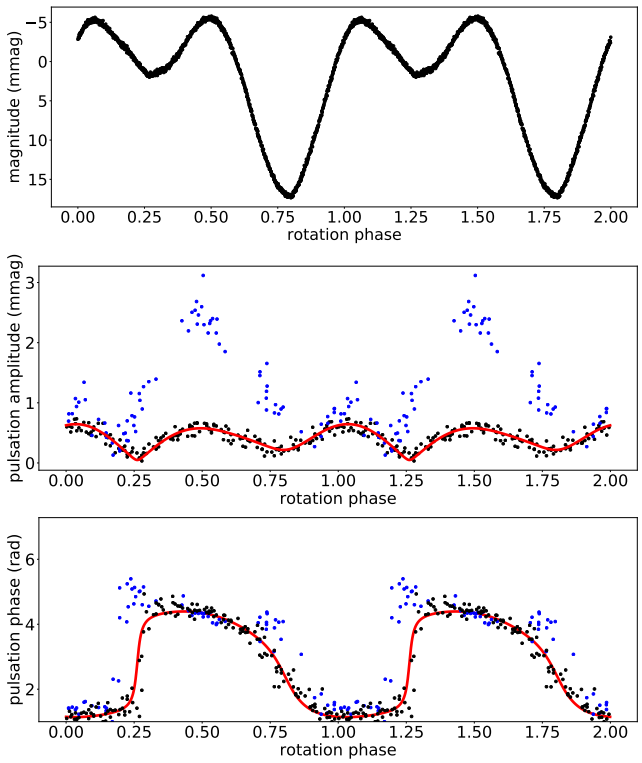

Figure 17. The same as Fig. 4 but for HD 6532. The black points are the data from TESS sector 3 observations and the blue points are from ground-based observations (Kurtz et al. 1996a).

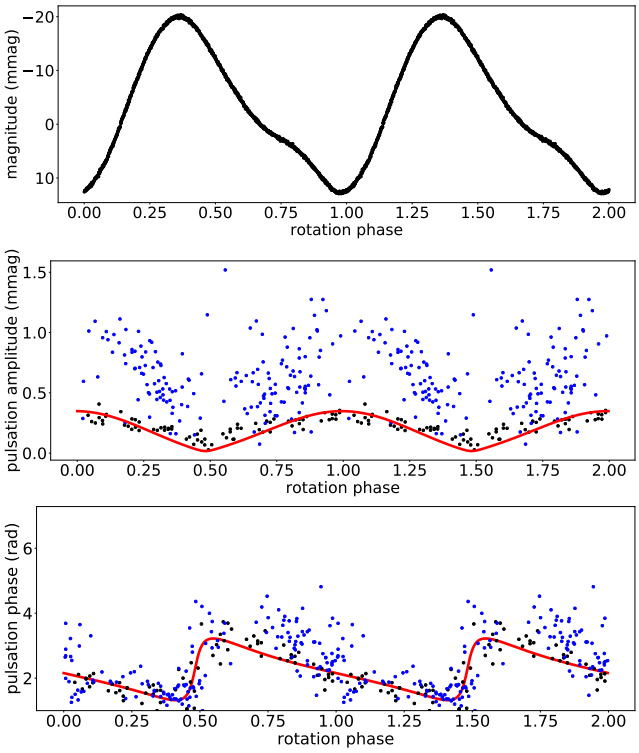

Figure 18. The same as Fig. 4 but for HD 80316. The data are from TESS sector 8 observations.

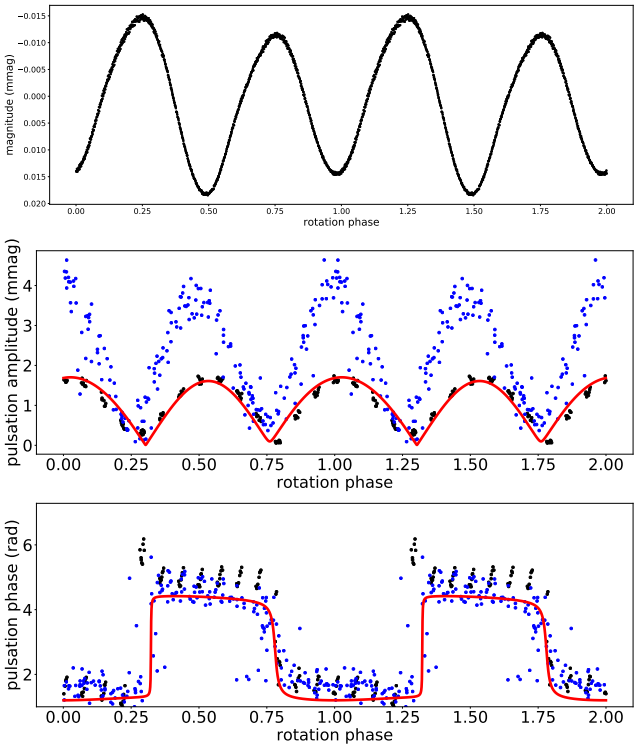

Figure 19. The same as Fig. 4 but for HR 3831. The black points are the data from TESS sector 9 observations and the blue points are from ground-based observations from Kurtz et al. (1997b).

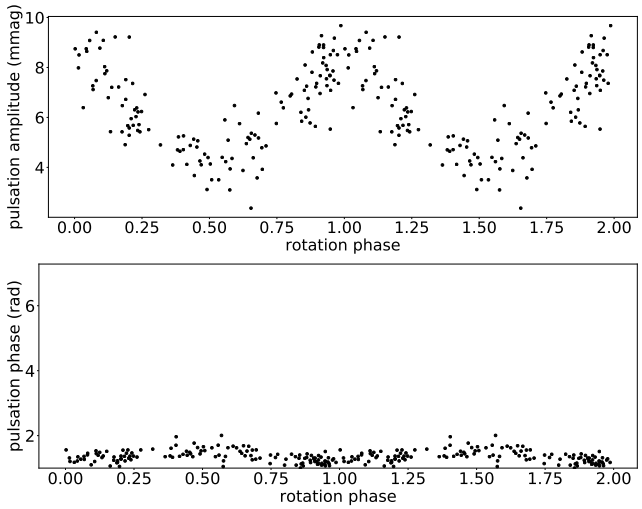

Figure 20. The same as Fig. 19 but for J1640. The data are from Holdsworth et al. (2018b). There is no data from space telescope for this star.